International Journal of Heat and Mass Transfer 52 (2009) 3906–3917

Contents lists available at ScienceDirect

International Journal of Heat and Mass Transfer

journal homepage: www.elsevier.com/locate/ijhmt

3D Simulations to investigate initial condition effects on the growth of Rayleigh–Taylor mixing

Arindam Banerjee [a,*], Malcolm J. Andrews [b,1]

[a] Missouri S&T [2], Department of Mechanical & Aerospace Engineering, 213 Toomey Hall, Rolla, MO 65409, USA
[b] Los Alamos National Laboratory, P.O. Box 1663, Mail Stop D413, Los Alamos, NM 87545, USA

ARTICLE INFO

Article history:
Received 11 December 2008
Accepted 23 March 2009
Available online 4 May 2009

Keywords:
Instabilities
Rayleigh–Taylor
ILES
Initial conditions

ABSTRACT

The effect of initial conditions on the growth rate of turbulent Rayleigh–Taylor (RT) mixing has been studied using carefully formulated numerical simulations. An implicit large-eddy simulation (ILES) that uses a finite-volume technique was employed to solve the three-dimensional incompressible Euler equations with numerical dissipation. The initial conditions were chosen to test the dependence of the RT growth parameters (α_b, α_s) on variations in (a) the spectral bandwidth, (b) the spectral shape, and (c) discrete banded spectra. Our findings support the notion that the overall growth of the RT mixing is strongly dependent on initial conditions. Variation in spectral shapes and bandwidths are found to have a complex effect of the late time development of the RT mixing layer, and raise the question of whether we can design RT transition and turbulence based on our choice of initial conditions. In addition, our results provide a useful database for the initialization and development of closures describing RT transition and turbulence.

Published by Elsevier Ltd.

1. Introduction

Rayleigh–Taylor (RT) instability [1–3] occurs when a light fluid (ρ_1) accelerates a heavy fluid (ρ_2) in the presence of infinitesimal interfacial perturbations h_0 of wavelength $\lambda = 2\pi/k$ at the interface. The instability is of interest due to its impact in such fields of study as climate dynamics [4,5], combustion and chemical reactor processes [6,7], pollutant dispersion [8], Inertial Confinement Fusion (ICF) [9,10], and cosmic and stellar dynamics [11,12]. At early times, for small enough initial perturbations ($h << 1/k$), the flow can be described by linear analysis [13] and the amplitude grows exponentially according to:

$$h(t) = h_0 \cosh(\Gamma t), \tag{1}$$

where, $\Gamma = \sqrt{A_t g k}$ is the classical growth rate, and the Atwood number $A_t = (\rho_1 - \rho_2)/(\rho_1 + \rho_2)$ is the non-dimensional density contrast between the two fluids. When the flow transitions to nonlinearity ($h \sim 1/k$), the growth slows down and the amplitude increases linearly with time. In this regime, the flow evolves into bubbles of lighter fluid rising through the heavy fluid with a terminal velocity $\propto \sqrt{\lambda}$ for a single mode [14,15], and corresponding spikes of heavy fluid falling through the light fluid. In the presence of a spectrum of modes, the RT flow is dominated by successively longer wavelengths of the dominant bubbles λ_b. For a constant acceleration, the mixing width growth attains self-similarity (i.e., as the bubbles grow they preserve their aspect ratio) such that the mixing width grows quadratically [16,17] with time according to the relation:

$$h_{b,s} = \alpha_{b,s} A_t g t^2, \tag{2}$$

h_b and h_s are the heights (above/below the initial density interface) of "rising" bubbles and "falling" spikes, respectively; α_b and α_s denote growth rate parameters (for the bubbles and spikes). The implication of Eq. (2) is that the flow has lost memory of the initial conditions and the only relevant length scale is the self-similar scale Agt^2. However, universal values of the growth parameters has eluded both numerical and experimental investigation, and has been attributed to the variations in the structure of the initial conditions employed in experiments and simulations [18,19]. Physically, self-similarity in RT can generally be achieved through two limiting scenarios: bubble merger and/or bubble competition [19,20]. Bubble merger occurs when two or more bubbles merge to form a larger structure that then undergoes a second generation of mergers and so on. In bubble competition, amplification and saturation of successively longer wavelengths, already present in the initial spectrum, dominates the flow. Haan [14] considered the constructive interference experienced by adjacent modes in a wave-packet, triggering transition when the sum of modal amplitudes in the wave-packet is $\sim\sigma/k$ (σ being a non-linear threshold). Thus, individual modes may become non-linear even when their

* Corresponding author. Tel.: +1 573 341 4494; fax: +1 573 341 4607.
E-mail addresses: banerjeea@mst.edu (A. Banerjee), mandrews@lanl.gov (M.J. Andrews).
[1] Tel.: +1 505 606 1430; fax: +1 505 665 4972.
[2] Formerly University of Missouri-Rolla.

0017-9310/$ - see front matter Published by Elsevier Ltd.
doi:10.1016/j.ijheatmasstransfer.2009.03.032

Nomenclature

Alphabetical listing

a_k, b_k, c_k, d_k	spectral amplitudes
f	volume fraction
g	gravity
h_b	mix width: bubbles
$h_{s;}$	mix width: spikes
h	total mix-width $h = h_b + h_s$
k	wave-number
p	pressure
p_s	spectral index
t	time
u, v, w	velocity components
x, y, z	spatial co-ordinates
Δx, Δy, Δz	cell-widths
Δt	time step
A_t	Atwood number
W	integral mix width

Greek symbols

α	growth-parameters
χ	ratio of KE
Δ	size of computational cell
ε_e	$=\Delta tu/x$
ν	viscosity
Γ	linear growth rate
θ	molecular mix parameter
Λ	ratio of mean square amplitudes

Subscript

0	initial value
1,2	heavy, light
b,s	bubble, spike
x, y, z	co-ordinates
e, n, s, w	face values (e: east, w: west, etc.)
E, N, S, W	cell center values (e: east, w: west, etc.)
max	maximum value
total	total value

Superscript

$*$	intermediate value
‘	*rms* value

amplitudes are below the threshold due to their interaction with adjacent modes of similar phase. We can interpret Eq. (2) to be the quadratic envelope of the growth curves of all such individual modes [20]. By changing the initial amplitudes of these modes, we may cause them to saturate earlier (or later), and thus the slope of this envelope (α_b) can be changed. Since the disturbances grow exponentially up to saturation, the time to nonlinearity (and thus α_b) depends logarithmically on the initial amplitudes.

Youngs [21] performed large-eddy simulations (LES) of RT at a resolution of $720 \times 480 \times 480$, initialized with a spectrum that had energy only in the high mode-numbers (90–180). The flow evolved with a growth rate of $\alpha_b \sim 0.027$, which doubled to $\alpha_b \sim 0.057$ with the addition of a single long wavelength in the initial spectrum at a mode-number of 2. Cabot and Cook [22], in their large (3092^3) direct numerical simulations (DNS) at a maximum Reynolds number (defined as $Re = h\dot{h}/\nu$) of $\sim 3 \times 10^4$, studied the effect of the initial spectral peak (k=k_{max}) on the growth rate. They report self-similarity only for the case with the highest value of the peak wave-number k_{max}. Their plots of α_b asymptotes to a value of 0.025 which is much lower than the corresponding values obtained from experiments. The DNS of Young et al. [23] used an annular spectrum that evolved through mode-coupling and gave $\alpha_b \sim 0.03$. Simulations in which numerical diffusion is suppressed through a Front-Tracking technique [24] found a higher value for $\alpha_b \sim 0.07$. Thus, while most numerical simulations are initialized with annular spectra, experiments have inherent long-wavelength content in their initial conditions [25–27]. Ramaprabhu and Andrews [18] initialized RT simulations with initial conditions that contained long wavelengths measured directly from their Water Channel [26], and found good agreement between the experimental and numerical values of α_b. Similar long wavelength perturbations have also been observed in the experiments of Banerjee et al. [25] and Dimonte and Schneider [27], suggesting that experiments do not evolve purely through the bubble merger mechanism. Ramaprabhu et al. [19] suggests that these two processes (bubble merger and bubble competition) exist simultaneously in experiments and are in competition, or perhaps they are complimentary. The current work examines the concepts described above through three-dimensional numerical simulations with carefully imposed initial conditions. We explore possible influences on the growth rates with simulations that have annular spectra at different amplitudes. Effects associated with variation of this annular spectrum, such as: the spectral shapes (referred to as the Spectral Index (p_s) herein, and quantified as the exponent of the wave-number i.e., $h_0 = k^{p_s}$); and, effects of spectral width and discretely banded spectra imposed on the initial condition are also investigated. The remainder of the paper is organized as follows. In Section 2 we describe the governing equations and the numerical algorithm. Details of the computational setup are provided in Section 3. Results from a multi-mode study are described in Section 4 followed by discussion and conclusions in Section 5.

2. Governing equations and numerical details

2.1. Governing equations

The incompressible Euler equations are used in conjunction with the ILES (see below for more details) modeling technique:

$$\text{Volume conservation}: \nabla \bullet \underline{u} = 0 \tag{3}$$

$$\text{Scalar transport}: \frac{Df}{Dt} = 0 \tag{4}$$

$$\text{Momentum}: \frac{D(\rho \underline{u})}{Dt} = -\nabla p + \rho \underline{g} \tag{5}$$

with the fluid velocity $\underline{u} = (u, v, w)$, density, ρ, pressure, p, and gravity, $\underline{g} = (0, 0, g_z)$, and scalar f. There are six independent variables and five equations; the sixth equation is a linear equation of state for density such as $\rho = L(f)$. In the present work we take f to be the non-dimensional density, or mixture fraction, defined as $f = (\rho - \rho_2)/(\rho_1 - \rho_2)$.

2.2. Numerical solution procedure

2.2.1. Overview

For the present studies we have used ILES (implicit large-eddy simulation) modeling which involves solving Euler governing equations and uses numerical diffusion to model turbulent diffusion. Success with this modeling technique for buoyancy driven flows has been reported by Youngs [21]. The governing equations

presented above are a coupled set of partial differential equations for which there exist several solution procedures. The present work solves the governing equations using the RTI-3D code described by Andrews [28]. In particular, a fractional time step technique is used in which for each time step an advection calculation is followed by a Lagrangian source term update. The Lagrangian update is presented next, and this is followed by a brief description of the advection step for the scalar f (more details about the technique may be found in Andrews [28], and Andrews Ph.D. Thesis [29]).

2.2.2. Lagrangian momentum source term updates

The Lagrangian w momentum equation is:

$$w_n^* = w_n^{n+1/2} + \frac{\Delta t}{\rho_t \Delta y}(p_P^n - p_T^n) + g_z \tag{6}$$

The $n + 1/2$ superscript refers to a value from the advection calculation, and $*$ to an intermediate value that does not necessarily satisfy continuity. The subscripts refer to spatial position (north face), typical of the SIMPLE method [30], and a staggered arrangement of momentum and mass cells is used. Following the SIMPLE practice, velocity corrections are defined so that $u_{i,e}^{n+1} = u_{i,e}^* + \Delta u_{i,e}$ (and similarly for the other velocities) and a new pressure $p_P^{n+1} = p_P^n + \Delta p_p$ where Δp is a pressure correction. By substituting these expressions for $n + 1$ into the volume conservation equation and then subtracting Eq. (6) evaluated with the $*$ we arrive at the usual Poisson equation for pressure corrections:

$$a_P \Delta p_P + a_E \Delta p_E + a_W \Delta p_W + a_N \Delta p_N + a_S \Delta p_S = -Div \tag{7}$$

with Div the divergence of the $*$ velocity values. The Poisson Eq. (7) is solved using a Full Multi-Grid method, and the pressure corrections are used in a SIMPLE style [30] to provide updated $(n + 1)$ velocities and pressures that simultaneously satisfy the momentum Eq. (5) and volume conservation.

2.2.3. Transport procedures

The 3D transport procedures are split into $x/y/z$-steps, this fractional splitting simplifies the calculation to one-dimensional updates that lends itself to high order calculation of cell fluxes with the Van Leer [31] method. There follows a brief description of the scalar x-step advection, the y- and z-steps being similar, and similar advection steps are performed for the momentum. The x-step advection for the scalar is given by:

$$f_P^* = f_P^n + \Delta y \Delta z \Delta t (u_e f_e - u_w f_w) \tag{8}$$

where P refers to the center of a control volume, e the east face, and w the west face. The face values for the u velocities are available, and the face values for the scalar are computed using a second order approximation with Van Leer limiting to prevent non-physical oscillation as:

$$f_e = f_{\text{upwind}} + \text{sign}(\varepsilon_e)\frac{(1-\varepsilon_e)}{2}\Delta x D_e \tag{9}$$

where $\varepsilon_e = \Delta t u_e / \Delta x$, and upwind values are taken according to the sign of ε_e. The derivative is evaluated following Van Leer [31] as:

$$D_e = S \min\left\{|D|, \frac{2|\Delta_w|}{\Delta x}, \frac{2|\Delta_e|}{\Delta x}\right\} \tag{10}$$

where $\Delta_w = f_P^n - f_W^n$, $\Delta_e = f_E^n - f_P^n$ and $S = \begin{cases} 1 & \text{if } \Delta_e \text{ and } \Delta_w > 0 \\ -1 & \text{if } \Delta_e \text{ and } \Delta_w < 0 \\ 0 & \text{otherwise} \end{cases}$.

Van Leer limiters have been used in Eq. (10) to limit the gradient of the volume fraction profile, thereby preventing spurious oscillations. The representation for the gradient of the cell profile D determines the accuracy of the representation. In the present work $D = (\Delta_e + \Delta_w)/(2\Delta x)$, so the gradient is computed with a central difference so this scheme is referred to as "second-order". Of significant importance in the simulation of R–T flows is the convection calculation of the fluxes of mass and momentum. A third-order Van Leer method [31] used to compute convective fluxes, minimizes numerical diffusion and prevents spurious overshoots and undershoots that occur due to the use of higher order numerical schemes. A two-phase, 2D version of this code was tested and validated for both RT and Kelvin–Helmholtz flows by Andrews [27]. The 3D, single-phase version was used extensively [18–20] to compute both the single-mode and multi-mode RT problem, and compared well with other benchmark codes commonly used in the study of RT. Over the last 30 years, great progress has been made in the development of numerical methods employed in the study of RT flows. However, numerical diffusion has served to degrade the resolution and accuracy of these methods. This numerical diffusion is now being taken advantage of through the ILES technique [21].

While *RTI-3D* solves the Euler equations with no explicitly specified viscosity, numerical diffusion serves to dissipate small scales in a similar manner to physical viscosity. Such numerical techniques referred to as ILES have been demonstrated to be particularly attractive for flows with discontinuities (RT) and shocks (as in Richtmyer–Meshkov (RM) Instability) [21]. The effective numerical viscosity of the ILES technique used here was determined through comparison of single-mode simulations with linear theory results [13]. Details about the technique used may be found elsewhere [19,20]. The implication of a numerical viscosity for multi-mode simulations is that similar to a physical viscosity, it sets an upper bound for the fastest growing modes. Smaller wavelengths, present in the initial conditions, or generated through non-linear interactions (mode-coupling), are smeared out by the numerical viscosity.

3. Problem set up and computational details

Fig. 1a is a schematic of the computational domain used in the current work. The dimensions of the three-dimensional box are $1 \times 1 \times 2$ m ($L \times L \times 2L$) in the x-, y- and z-directions, respectively, (where z is the direction of gravity). The interface between the heavy (ρ_1) and light (ρ_2) fluids is at $z = 0$. The densities were chosen to be $\rho_1 = 3.0$ kg/m^3 and $\rho_2 = 1.0$ kg/m^3 which corresponds to $A_t = 0.5$, while the acceleration due to gravity g_z was set to be -9.81 ms^{-2}. Perturbations $h_0(x, y)$ are imposed at the interface ($z = 0$) as fluctuations of a constant density surface (see Fig. 1b). These are then converted to volume fraction fluctuations using:

$$\begin{aligned} f_1(x,y) &= 1 + h_0(x,y)/\Delta, \quad \text{for } h_0 < 0 \\ f_1(x,y) &= h_0(x,y)/\Delta, \quad \text{for } h_0 > 0 \end{aligned} \tag{11}$$

where Δ is the width of the computational cell. The pressure is initialized to the hydrostatic value in this incompressible problem using, $p(z) = -\int \rho g dz$, where $\rho = f_1\rho_1 + f_2\rho_2$, is the unperturbed initial density field. This is an important initial condition to set, because without it the algorithm will seek to establish the hydrostatic condition on the first time step, involving hundreds, if not thousands, of iterations for the pressure correction calculation. If an initial hydrostatic pressure field is provided, only three or four iterations are required on the first time step for pressure convergence. Periodic boundary conditions were used in the x- and y-directions, while zero-flux conditions were imposed in the z-direction. All the simulations reported here used a resolution of $128 \times 128 \times 256$ grid points (totaling 4.2 million cells) in the x-, y- and z-directions, respectively. The calculations were stopped when the bubble height reached $\sim$0.9 m to avoid boundary effects. The simulations were executed on the NIC Cluster at Missouri S&T. The run-times averaged around 3 CPU hours per calculation. Each of these simulations

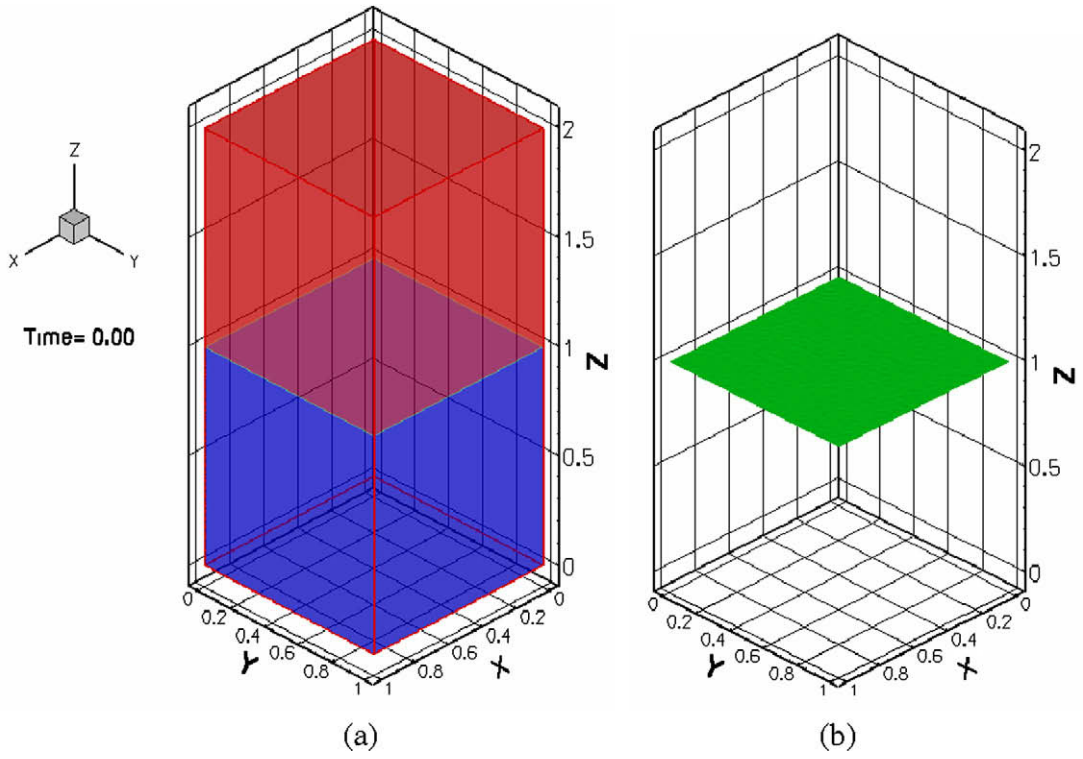

Fig. 1. Schematic of (a) computational domain used in NS. The box size is $1 \times 1 \times 2$ m (in the x-, y- and z-directions) with densities $\rho_1 = 3.0$ kg/m^3, $\rho_2 = 1.0$ kg/m^3 and $g_z = -9.81$ ms^{-2}; (b) location of density perturbations imposed on the interface at $t = 0$.

required 2GB of RAM and ~4GB of storage. The grid independence study indicates little change with increasing resolution (see Table 1) of the reported parameters in this work. Similar grid-independence for related ILES has also been demonstrated by Youngs [21].

3.1. Multimode calculations – initial conditions

The multimode calculations were designed to test the dependence of the growth constant α_b on the spectral index, spectral bandwidth, discrete spectral shapes and mode coupling. Modes 16–32 are selected for the mode coupling case to able cross comparison of the present simulations with the α-group results [20]. Dimonte et al. [20] suggests that this mode coupling case is least sensitive to initial conditions because it involves the non-linear coupling of saturated high-k modes of intrinsic scales $h \sim 1/k$. To assure that the low-k modes are generated exclusively by mode coupling, the initial perturbations are chosen to have finite amplitudes only in an annular shell in k-space at the largest resolvable wave numbers (see Fig. 2), namely, modes 16–32 for the $128 \times 128 \times 256$ simulations [20]. The initial perturbations are taken to be:

$$h(x,y) = \sum_{k_x,k_y} a_k \cos(k_x x)\cos(k_y y) + b_k \cos(k_x x)\sin(k_y y) + c_k \sin(k_x x)\cos(k_y y) + d_k \sin(k_x x)\sin(k_y y) \quad (12)$$

Table 1
Test of grid independence (IC Modes 16–32; $p_s = 0$). All simulations reported in this work had a grid size of $128 \times 128 \times 256$.

Grid size	$\alpha_{b,s} = \frac{dh_{b,s}}{d(A_t g t^2)}$		$KE_{total}/\Delta PE$	θ
	α_b	α_s		
$64 \times 64 \times 128$	0.0216	0.0283	0.521	0.826
$128 \times 128 \times 256$	0.0219	0.0263	0.499	0.833
$256 \times 256 \times 512$	0.0244	0.0266	0.485	0.814

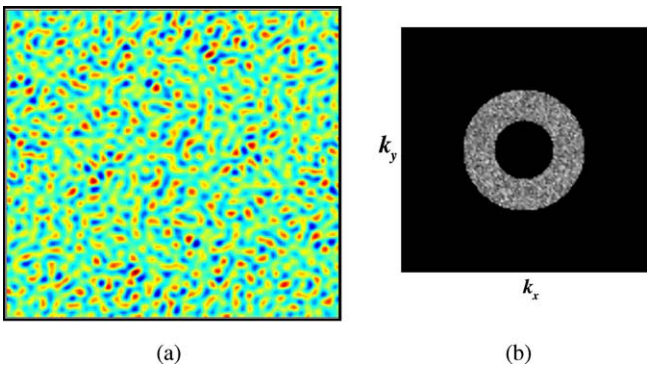

Fig. 2. Initial perturbations (at $z = 0$ in Fig. 1b) for simulation 1 in (a) physical, and (b) wave-number space.

where $k = \sqrt{k_x^2 + k_y^2}$, and the spectral amplitudes are chosen randomly but give an *rms* amplitude of $\sim 3.15 \times 10^{-4}$ L. Fig. 2a and b show the multimode perturbation amplitudes in both physical and wave-number space. Table 2 is a list of all the numerical simulations (NS) presented in this work. Simulations 1–3 were

Table 2
List of simulations reported in the current work.

Case #	IC modes	SI (p_s)
1	16–32	0
2	16–32	+1
3	16–32	−1
4	8–32	0
5	2–32	0
6	4–6 and 16–32, $\Lambda = 5$	0
7	4–6 and 16–32, $\Lambda = 50$	0
8	4–6 and 16–32, $\Lambda = 100$	0

performed to study the effect of Spectral Index on the RT growth. These calculations had energy in mode numbers ($n = kL/2\pi$) 16–32, but had spectral indices (p_s) of -1, 0 (white noise, α-group IC case) and 1. A spectral index of 1 corresponds to more energy in the high mode-numbers as compared with a spectral index of 0 (white noise). Correspondingly, calculations with spectral index of -1 had more energy in the low mode-numbers as compared with the other cases (i.e., $p_s = 0$ and 1). Simulations 4–5 were initialized with the smallest mode-numbers (longest wavelength) $N_{min} = 2$ and 8; the objective being to study the effect of spectral bandwidth on the growth parameters. The energy density spectrum has the canonical property:

$$\frac{\overline{h_0'^2}}{2} = \int_{k_{\min}}^{k_{\max}} E_{h0}(k)dk. \tag{13}$$

Thus, all the simulations were initialized with the same perturbation *rms* amplitude (h_{rms}), thereby ensuring that all the simulations had the same initial energy. Similarly cases 6–8 take into account the effect of discrete banded spectra. Energy was deposited in two concentric bands between mode numbers 4–6 and 16–32. Care was taken to ensure that the total energy used for these simulations was identical to the energy used in cases 1–5 by re-writing Eq. (13) for a banded spectrum such that:

$$\frac{\overline{h_0'^2}}{2} = \int_{k_{\min}}^{k_{\max}} E_{h0}(k)dk = \int_{k_{\min}}^{k_1} E_{h1}(k)dk + \int_{k_2}^{k_{\max}} E_{h2}(k)dk = \frac{\overline{h_1'^2}}{2} + \frac{\overline{h_2'^2}}{2}. \tag{14}$$

The ratio of the mean square amplitudes ($\Lambda = \overline{h_2'^2}/\overline{h_1'^2}$) in the two concentric bands were varied to test the influence of the small mode-numbers on the simulations. Cases 6–8 are simulations that correspond to $\Lambda = 5$, 50 and 100, respectively. Fig. 3 shows the azimuthally averaged initial perturbations for all the simulations (1)–(8). We also address the issue of the peak wave-number in the presence of numerical viscosity in these simulations. Numerical viscosity (similar to other stabilizing mechanisms like surface tension) places an upper bound on the fastest growing wave-numbers. The peak wave-number k_p may be determined as [32,33]:

$$k_p \approx 0.5\left(\frac{A_t g}{\nu^2}\right)^{1/3} \tag{15}$$

with a peak growth rate of $\sim 0.4(g^2/\nu)^{1/3}$. From the above, the fastest growing mode number for the current simulations was determined to be $N_p \sim 24$ [20], and within the range of modes imposed in our initial conditions. This guarantees that the linear growth stage is reproduced accurately by these calculations. Most numerical simulations of RT [19–23] are initialized with a similar annular distribution of energy. It is expected that the mode-coupling cases will produce a much lower growth rate than the simulations initialized with the longer modes [20], because the long wavelengths dominate the flow at late time. The cases reported in this work are listed below:

i. *Spectral index study*: cases 1–3 (note that case 1 is similar to α-group M128 simulation and is treated as a base case for comparison purposes).
ii. *Spectral bandwidth study*: cases 4 and 5.
iii. *Effect of discrete banded spectra*: cases 6–8.

4. Results

In this section, we analyze the 3D data fields from each of the numerical simulations described above (cases 1–8) to quantify growth rate, self-similarity, molecular mixing and energy dissipation for comparison with experiments and previous RT simulations.

The fluid penetration is characterized in terms of the species concentration or volume fraction of the "heavy" fluid f_1 averaged in the span-wise direction such that:

$$< f_1 >= \int\int f_1 dxdy/L^2 \tag{16}$$

Vertical profiles of $\langle f_1 \rangle$ are shown in Fig. 4 for (a) early, and for (b) late times for simulations 1–3. The profiles are nearly linear and symmetric, characteristic of the moderate Atwood number of 0.5 used in these simulations [17,20,25]. The evolution of the mixing zone is also depicted for case 1 in Fig. 5a by the iso-surfaces of f_1 at $A_t g t^2/L = 5.31$ and 19.62, respectively. At early time, there are numerous bubbles with wavelengths larger than the imposed modes, and that correspond to the most unstable mode. As the bubbles penetrate, the flow becomes self similar and the bubbles increase in size. A similar phenomenon may also be observed from the iso-surfaces of spikes at these moderate Atwood numbers (see Fig. 5b). Fig. 6 shows the evolution of the bubble and spike amplitudes as a function of a non-dimensional self-similar length $A_t g t^2/L$. The bubble and spike amplitudes h_b and h_s are defined by the *z*-location where the plane averaged values of $\langle f_1 \rangle$ reaches values of 99% and 1% volume fractions, respectively, relative to the original mid-position of the interface ($z = 0$). We also observe a ratio of $h_s/h_b \sim 1.25$ at late time which is consistent with the experimental observations [25–27] and with NS [19] at $A_t = 0.5$. The bubble and spike amplitudes are subjected to statistical fluctuations, especially at late time when there are few bubbles and spikes. To account for this problem, we also plot the integral mix width (W) defined by Andrews and Spalding [3] as:

$$W = 6\int \langle f_1 \rangle \langle f_2 \rangle dz \tag{17}$$

which measures the overlap of the heavy $\langle f_1 \rangle$ and the light $\langle f_2 \rangle$ fluids where $f_1 + f_2 = 1$. The factor of six derives from considering the width of a linear profile [3]. At small to moderate Atwood numbers where $h_b \sim h_s$, we find that $W/h_{b,s} \sim 2$ which is consistent with earlier NS [19,20].

The growth-rate parameter α_b is measured by using the definition from Ristorcelli and Clark (2004), (RC) [34] who, through a self-similar analysis for small Atwood RT mixing, obtained an ordinary differential equation for the planar average of the mixing layer half-width h_b as:

$$\alpha_{b,RC} = \frac{\dot{h}_b^2}{4A_t g h_b}. \tag{18}$$

As an exact mathematical result (18) validates the form of heuristically derived equations [35,36] that resulted from phenomenological buoyancy-drag type models. For constant $\alpha_{b,RC}$, A_t and g, the solution to (18) (taking only the positive root as physically realizable) can be written as:

$$h_b = h_0 + 2\sqrt{\alpha_{b,RC} A_t g h_0}\, t + \alpha_{b,RC} A_t g t^2, \tag{19}$$

where h_0 is a virtual starting thickness, that effectively depends on how long it takes for the flow to become self-similar, which in turn depends on the spectrum of initial perturbations. The growth rate constants for both the bubbles and spiked are calculated based on this definition (Eq. (18)). To cross-compare our results with earlier simulations, we also calculate the growth-parameters based on a definition used by Read [37]; obtained by differentiating $h_{b,s}$ with respect to $A_t g t^2$. Since these definitions are applicable only when the flow becomes self-similar, the values of $\alpha_{b,s}$ listed in Table 3 were calculated for $A_t g t^2 > 10$, when almost all the NS cases (1)–(5) studied in this work became self-similar.

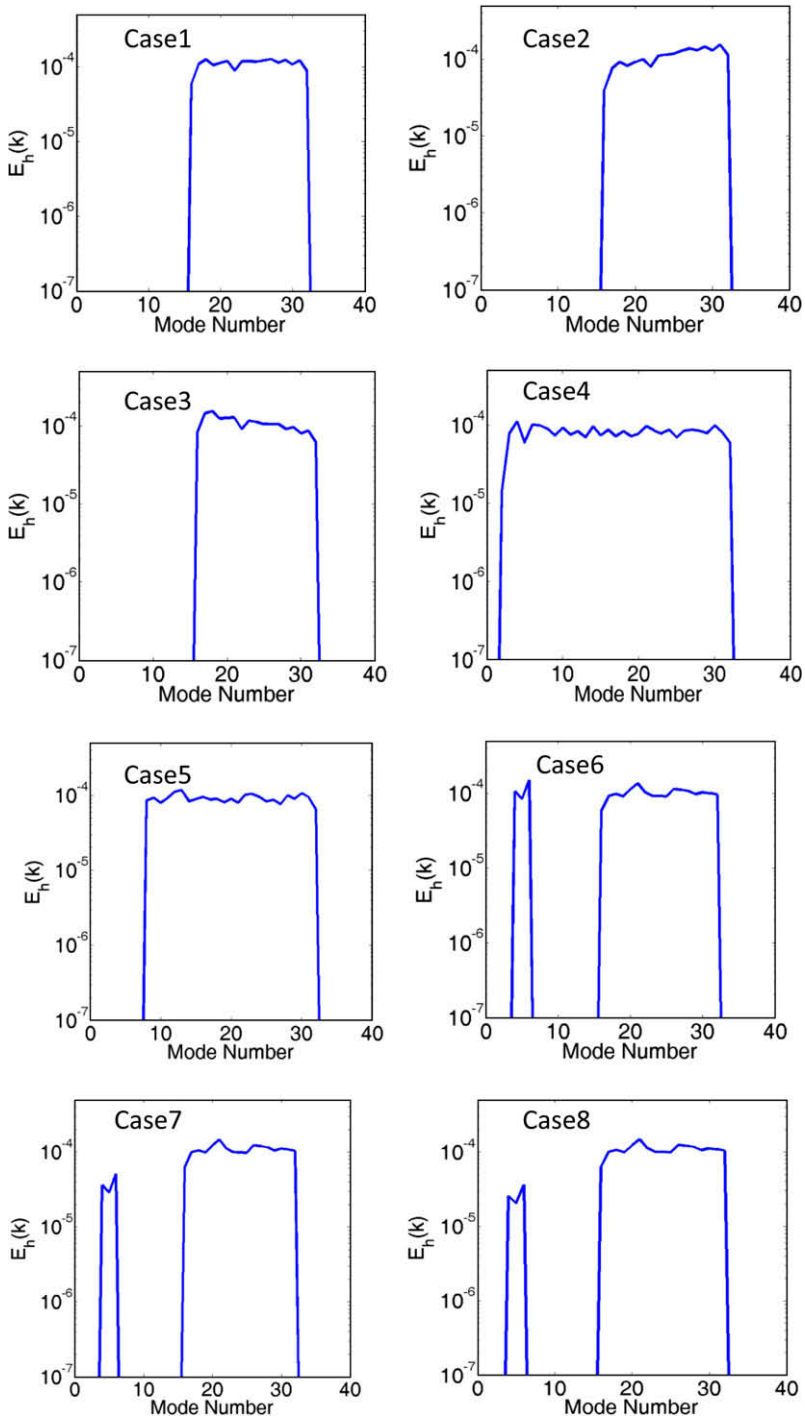

Fig. 3. Azimuthally averaged initial perturbations for all NS cases listed in Table 1. Root mean square amplitude is 3.15×10^{-4} *L*.

4.1. Effect of spectral index (p_s)

Cases 1–3 had the *rms* amplitude and energy in the same mode-number band (16–32) but spectral indices (p_s) = −1, 0 (white noise), and +1, respectively. From the time traces of h_b shown in Fig. 7, it may be observed that the p_s = +1 case (case 2) grew the fastest at early time as it has more initial energy at the high wave-numbers (see Fig. 7a). The p_s = −1 simulation (case 3) has the slowest growth as the NS is initialized with more energy in the low-amplitude, low wave-number (long wavelength), part of the spectrum sampled by the flow. The corresponding growth-parameters are plotted in Fig. 7b and show little sensitivity to p_s. Similarly, the time traces of h_s displayed in Fig. 7c show no sensitivity to the changes in the values of the spectral index p_s and the amplitudes of the spikes were almost identical at late time.

In addition to large-scale structures being felt in the bubbles and spike growth parameters, small-scale effects, namely the molecular mix parameter θ [38], were also investigated. Values for θ were computed from volume fraction profiles as:

$$\theta = \frac{\int \langle f_1 f_2 \rangle dz}{\int \langle f_1 \rangle \langle f_2 \rangle dz} \tag{20}$$

where $\langle \bullet \rangle$ denotes averaging over the *x*-*y* plane. θ approaches 1 for completely mixed fluids, and 0 for immiscible fluids. Thus, θ is a

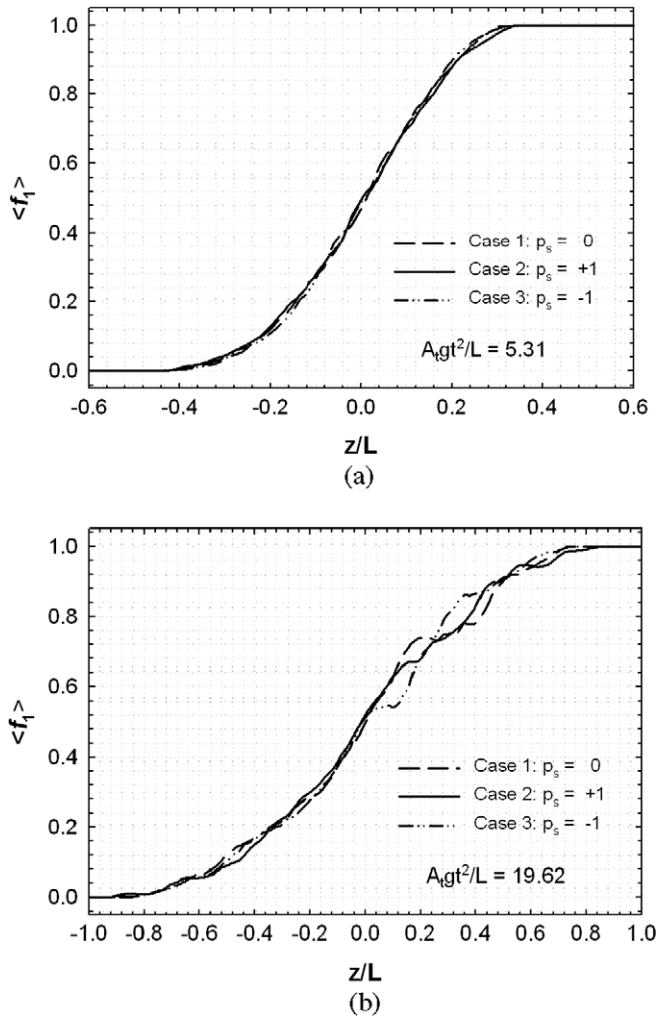

Fig. 4. Profiles of "heavy" fluid volume fraction averaged over horizontal planes at $A_t g t^2/L$ values of (a) 5.31 and (b) 19.62.

parameter that characterizes molecular mixing. The evolution of θ with Agt^2 is shown in Fig. 7 (d) for cases 1–3. For all these cases, θ asymptotes to a value of ~0.8 that is consistent with experiments [25,26,39]; although at slightly different rates. Interestingly the level of diffusion in ILES is expected to be higher than that due to true physical mass or momentum, however, the NS produces the a similar level of molecular mixing as experiments and high-resolution DNS. The high-resolution ILES study of Youngs [21] gave a value of 0.81 for θ in the self-similar stage. The ILES concept is that numerical diffusion captures the molecular mixing associated with unresolved small-scales implicitly in the numerical scheme, and our results support this conclusion for RT mixing.

4.1.1. Energy budget

Development of the RT flow into self-similarity involves the conversion of initially available potential energy to kinetic energy. The ratio of the kinetic energy of the flow to the accompanying loss in potential energy has been found to be nearly constant for such flows [19,20,25,26,40] at a value of 0.5. We use the approach outlined in [19] to define this ratio: assuming for low A, a linear profile of the volume fractions, and $h_s \sim h_b = h$, then the loss in potential energy may be written as

$$\Delta PE = \int_{-h}^{0} (\rho_1 - \langle\rho\rangle) g z dz + \int_{0}^{h} (\langle\rho\rangle - \rho_2) g z dz \approx \frac{(\rho_2 - \rho_1) g h^2}{6}. \tag{21}$$

In Eq. (21), the error in assuming $h_s \sim h_b$ results in an overall error in ΔPE of ±5% for the NS presented in this paper. The corresponding gain in kinetic energy is more difficult to evaluate because density and velocity fluctuations are correlated. However, if we replace the respective densities by their average, the average velocity can be estimated as $w \sim \dot{h}$, which gives a vertical kinetic energy of:

$$KE_z = \frac{1}{2L^2} \int_{-h}^{+h} \rho w^2 dx dy dz = \overline{\rho} \dot{h}^2 h \tag{22}$$

The ratio of Eqs. (21) and (22) gives:

$$\frac{KE_z}{\Delta PE} = 3 \frac{\dot{h}^2}{A_t g h} = 12 \alpha_{b,RC} \tag{23}$$

If there are no other energy sinks, i.e., $KE_z/\Delta PE \sim 1$, we can place an upper bound on $\alpha_{b,RC} \sim 0.083$. However, the dissipated energy D and kinetic energy in the horizontal directions KE_x and KE_y must also be considered when calculating the global energy balance as:

$$\Delta PE = KE_x + KE_y + KE_z + D \equiv KE_{total} + D \tag{24}$$

The total gain in kinetic energy (KE_{total}) can be evaluated by integrating over the entire computational domain:

$$KE_{total} = \frac{1}{2} \int \rho (\vec{V} \bullet \vec{V}) dx dy dz \tag{25}$$

The ratio $KE_{total}/\Delta PE$ is plotted for cases 1–3 in Fig. 8. The fraction of energy dissipated is given by $1\text{-}KE_{total}/\Delta PE$, and approaches a value ~0.55 for these simulations. This is in good agreement with recent experiments by the authors [25], where they report a value of $D/PE = 0.52$ from their simultaneous measurements of density and velocity fields using hot-wire anemometry. Fig. 8 is a plot of $KE_{total}/\Delta PE$ from all simulations in cases 1–3 and shows only a slight dependence on the spectral index. The ratio of the vertical to the horizontal components of kinetic energies, $X = (KE_x + KE_y)/KE_z$ from these simulations was determined to be ~0.61. In comparison, Youngs (1994) gives a value of ~0.48 for $KE_{total}/\Delta PE$ and ~0.7 for the ratio of kinetic energy components (X). These values are in good agreement with the experimentally observed values of 0.62 for X inferred from a velocity ratio of ~1.8 obtained from the hot-wire measurements [25]. Dimonte et al. [20] combined the energy balance in Eq. (24) with vertical kinetic energy expression of Eq. (23) to obtain a bound of α_b from the energy budget calculations as:

$$\alpha_b \sim \frac{KE_{total}/\Delta PE}{12[1+X]} \tag{26}$$

At early times, when energy dissipation is small, i.e. $KE_{total}/\Delta PE \sim 1$, a value of $\alpha_b \sim 0.053$ is obtained from the NS for case 1. With the observed ratio of $KE_{total}/\Delta PE \sim 0.49$ at late times, Eq. (23) yields a value of 0.0247 which is consistent with the NS results and the late time values of α_b plotted in Fig. 7b (for case 1).

4.2. Effect of spectral band-width

Ramaprabhu et al. [19] studied the effect of the longest wavelength imposed in the initial conditions by varying the smallest mode-number in the wave-packet, N_{min} from 1 to 3. The growth-rate parameter α_b was found to be insensitive to such variations. For much higher values of N_{min}, mode-coupling is expected to play a more dominant role, accompanied by a decrease in α_b. Cases 4 and 5 illustrate the effect of variation of spectral bandwidth of the IC on both the large scale (growth-constants, amplitude) and small-scale (molecular mixing, KE release) parameters in the RT mix. Cases 4 and 5 were initialized with N_{min} of 2 and 8 respectively, and with the same net initial energy as cases 1–3. Fig. 9 plots the values of $\alpha_{b,s}$ for the different values of N_{min}. Inspection

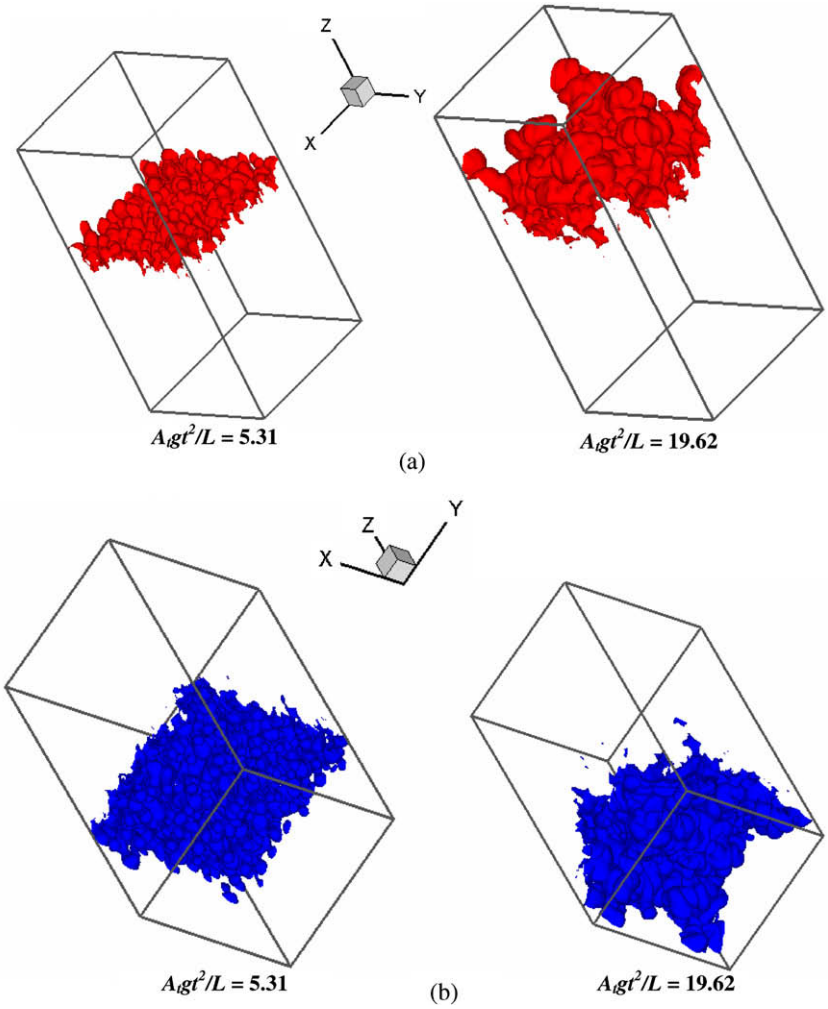

Fig. 5. Iso-surfaces of (a) f_1 (bubbles) (b) f_2 (spikes) at $A_t gt^2/L = 5.31$ and 19.62.

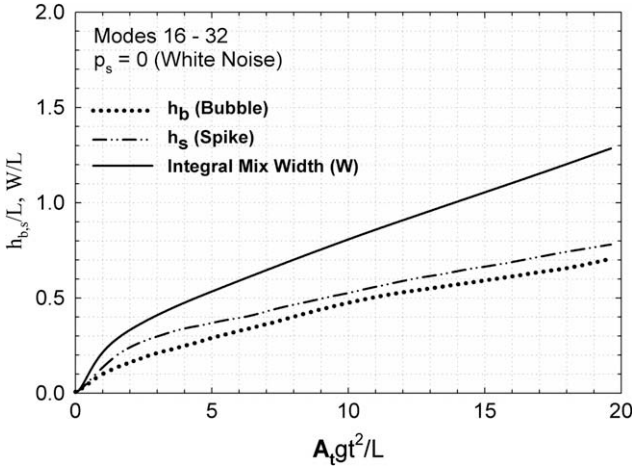

Fig. 6. Evolution of bubble and spike amplitudes (h_b and h_s), and integral mix width for case 1 (energy in modes 16–32 with SI = 0).

of Fig. 9 reveals that the growth parameters for the bubbles and spikes vary with the change in the minimum mode number. It is observed that the incorporation of longer wavelengths leads to an increase in α_b which asymptotes to a value of 0.023, which is consistent with cases 1–3. However, there appears to be no clear trend for α_s. Simulation 4 which is initialized with $N_{min} = 2$ is found to be the most efficient amongst cases 1–5 for extracting kinetic energy from the initial density distribution $KE_{total}/\Delta PE \sim 0.7$. This again suggests that the presence of long wavelengths is an efficient way to extract energy while minimizing dissipation. Indeed, it appears that there is a "critical" N_{min}, somewhere between 16 and 8 at which energy dissipation governs the flow. This simulation also had the largest growth-rate which implies the appearance of large-scale structures in the flow at early times. Thus, the rate of extraction of potential energy was much higher than that observed in simulations 1 and 5. The molecular mix parameter θ at late time is insensitive to the single banded structure (see Fig. 10), perhaps because all the simulations had high wave-number IC's that drives diffusion at the smallest scales resolved.

4.3. Effect of discrete banded spectra

Figs. 11–13 present the results from partitioned initial banded spectra, cases 6–8 of Fig. 3, and also shown for reference are the results for case 1 (the alpha group problem). Inspection of Fig. 11 reveals that cases 1 and 6 are remarkably similar, so it is evident that a missing band of wave-numbers is not recognized as the high wave-number band mode-couples to fill-in the missing domain, and the low wave-number modes retain their identity while waiting for the high wave numbers to develop. However, Fig. 11 shows that in cases 7 and 8 the mix width accelerates at about

Table 3
List of growth parameters, $KE_{total}/\Delta PE$ and θ for all simulations.

Case #	Ristorcelli and Clark (2004) definition $\alpha_{b,s} = \frac{h_{b,s}^2}{4A_t g h_{b,s}}$		α-group definition $\alpha_{b,s} = \frac{dh_{b,s}}{d(A_t g t^2)}$		$KE_{total}/\Delta PE$	θ
	α_b	α_s	α_b	α_s		
1	0.0229	0.0271	0.0219	0.0263	0.499	0.833
2	0.0270	0.0305	0.0241	0.0324	0.442	0.818
3	0.0349	0.0258	0.0304	0.0281	0.537	0.821
4	0.0285	0.0244	0.0276	0.0205	0.679	0.783
5	0.0224	0.0299	0.0181	0.0345	0.783	0.817
6	0.0302	0.0392	0.0306	0.0434	0.584	0.761
7	0.0406	0.0337	0.0493	0.0346	0.573	0.793
8	0.0461	0.0317	0.0554	0.0331	0.478	0.846

$A_t gt^2/L = 10$, and apparently there has been a transition in the development rate of the mixing region. We attribute this change in growth rate to the "late" appearance of the low wave-number (long wavelength) embedded in the initial conditions, associated with their reduced initial amplitudes that delays their appearance. This in-turn causes an extended period for the mode-coupling regime (that explains the slight reduction just before $A_t gt^2/L = 10$). The α_b measures of Fig. 12 plainly reveal the dramatically different growth rates associated with the partitioned energy spectra. The peak in case 8 suggests a narrowing of the energy budget into the long wavelengths at late time, associated with an increased dissipation of the short wavelength band. Again, the molecular mix parameter shown in Fig. 13 seems independent of the initial spectrum, because it is only dependent on the presence of the high wave-number band.

5. Conclusions

The effect of initial conditions on the growth of turbulent Rayleigh–Taylor (RT) instability has been studied using implicit large-eddy simulation (ILES). We have explored possible influences on the growth rate with simulations that are initialized with annular spectra at different amplitudes. The initial conditions were chosen to test the dependence of the RT growth parameters (α_b, α_s) on variations in spectral bandwidth, spectral shape, and study the effects of initially partitioned (banded) spectra.

Spectral indices (p_s) = −1, 0 (white noise), and +1 were chosen for testing. It was observed that the $p_s = +1$ case grew the fastest initially as it has more energy was initially in the high wave-numbers. The $p_s = -1$ simulation had the slowest growth as the NS was initialized with more energy in the low-amplitude, low wave-number, part of the spectrum sampled by the flow.

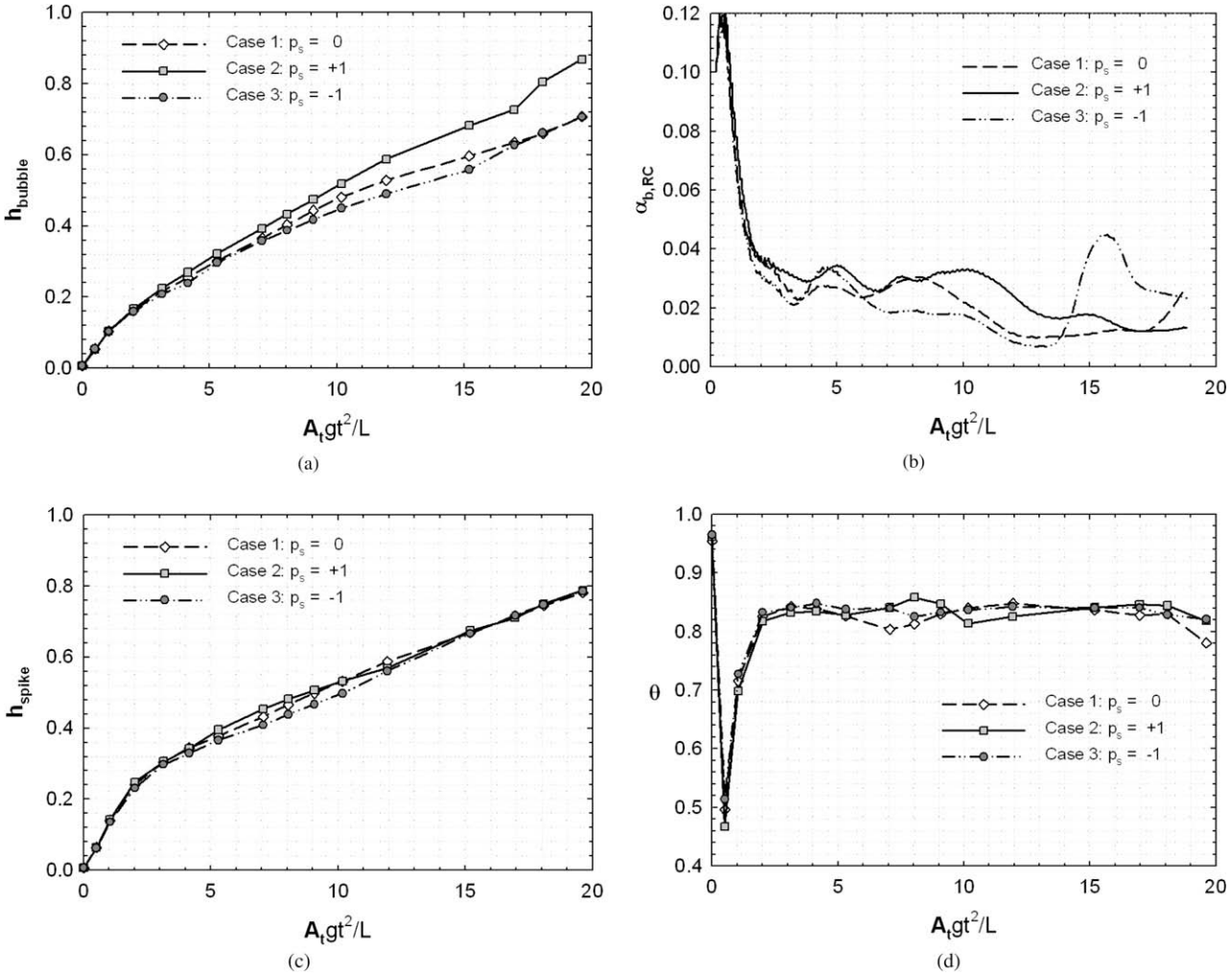

Fig. 7. Evolution of (a) bubble amplitudes, (b) growth-parameter for bubbles, (c) spike amplitudes, and (d) molecular mix parameter θ, for case 1 ($p_s = 0$), 2 ($p_s = +1$) and 3 ($p_s = -1$). All simulations had the same total energy in modes 16–32.

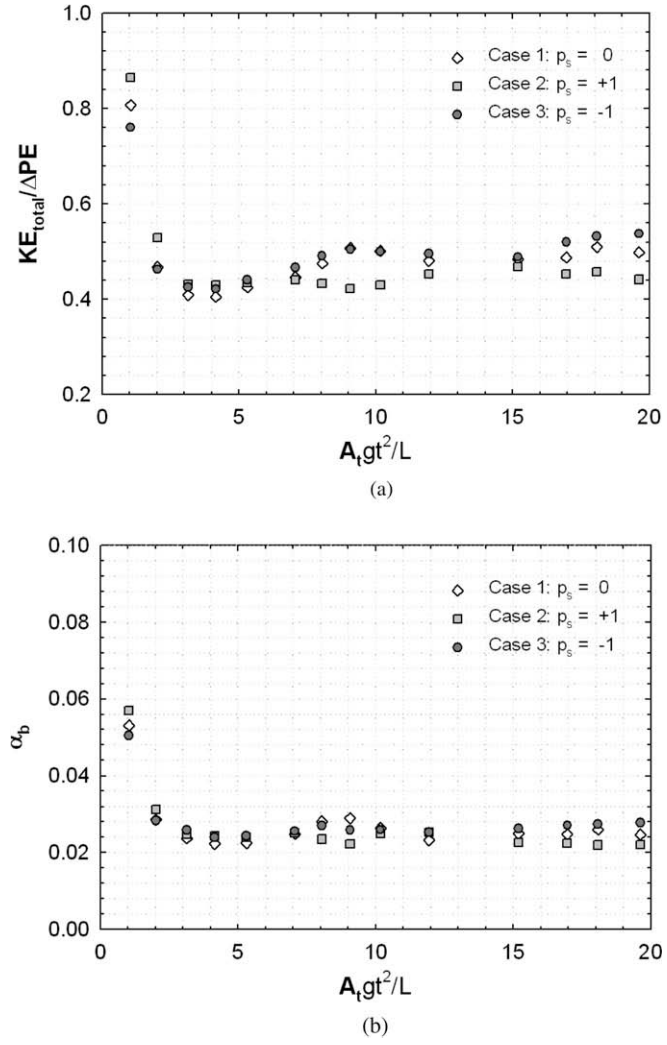

Fig. 8. Evolution of (a) $KE_{total}/\Delta PE$ and (b) α_b based on energy budget for cases 1–3.

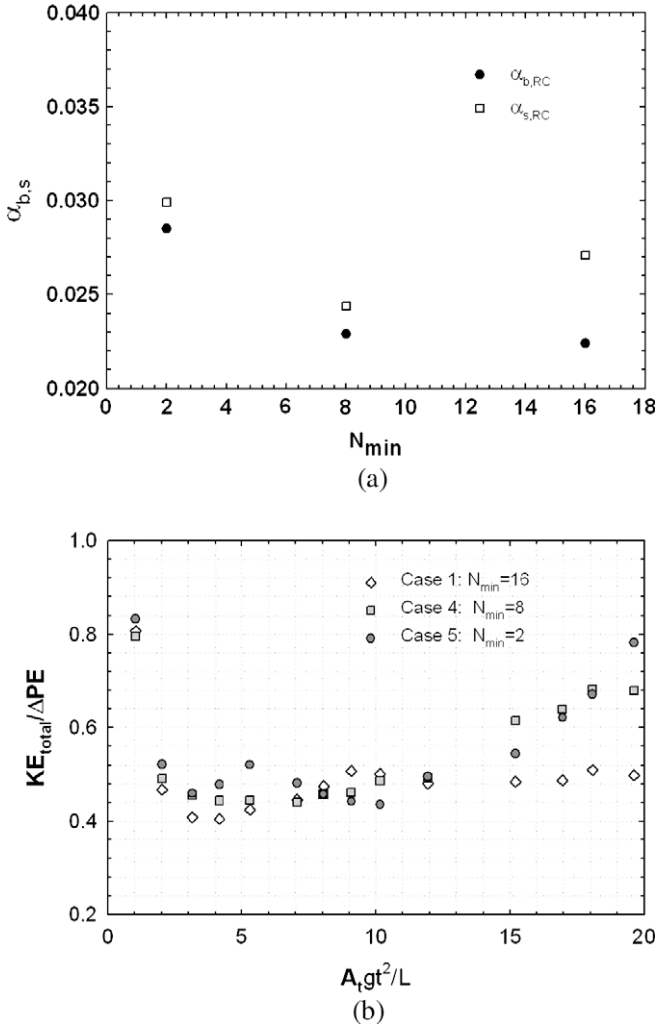

Fig. 9. Effect of longest wave-length (N_{min}) on (a) the growth parameters $\alpha_{b,RC}$ and $\alpha_{c,RC}$, and on (b) the $KE_{total}/\Delta PE$ for simulation initialized with N_{min} = 16, 8 and 2.

However, the growth parameters $\alpha_{b,s}$ showed no sensitivity to changes in the values of the spectral index p_s. In addition, the effect of the longest wavelength imposed in the initial condition was investigated by varying the smallest mode-number in the wave-packet such that N_{min} =2, 8 and 16. The growth parameters were found to vary with the change in the minimum mode number; the incorporation of longer wavelengths leads to an increase in α_b which asymptotes to a value of 0.023 for $N_{min} \geqslant 8$. For all these cases, the molecular mixing parameter θ remains insensitive to variations in IC's and was found to asymptote to a value of ~0.8 (consistent with experiments), perhaps because all the simulations had a high wave-number band in the IC's that promoted diffusion at the smallest resolved scales. The present ILES simulations produced the same level of molecular mixing as experiments and high-resolution DNS. The effect of partitioned initial banded spectra was also studied, and dramatically different late-time ($A_t gt^2/L > 10$) transition and growth rates were observed. The late appearance of the low wave-number modes embedded in the initial conditions, whose appearance is delayed by their reduced initial amplitude, was found to cause an extended period for the mode-coupling regime, and late-time accelerated growth of the mixing region.

Our findings further support the notion that the overall growth of the RT mixing is strongly dependent on initial conditions. The results also raise the possibility of design and active control of RT

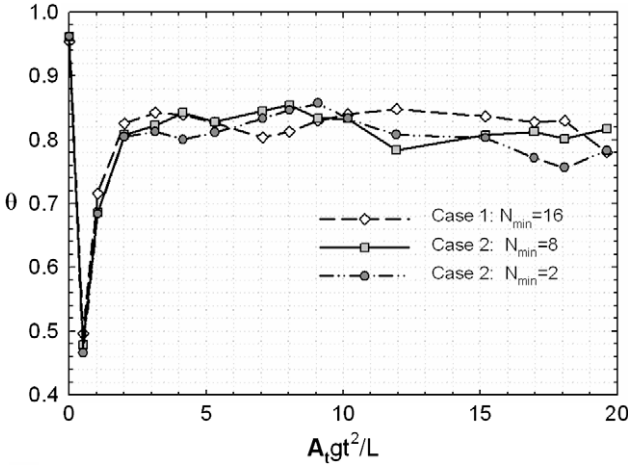

Fig. 10. Evolution of molecular mix parameter θ, for case 1 (N_{min} = 2, 8 and 16). All simulations had the same total energy with amplitude 3.15×10^{-4} L.

transition and turbulence, based on the choice of the shape and size of the initial perturbation spectrum. In addition, our results provide a useful database for the initialization and development of closures describing RT transition and turbulence.

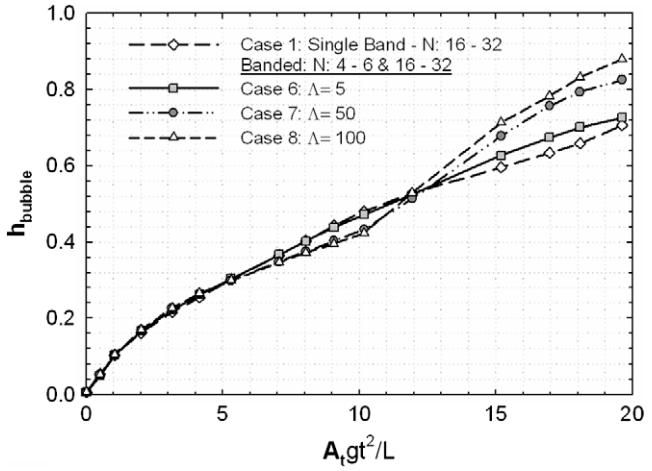

Fig. 11. Evolution of bubble amplitudes for case 1 (single band, N: 16–32) and cases 6–8 (double band, N: 4–6 and 16–32 with $A = 5$, 50 and 100, respectively). All simulations had the same total energy at $t = 0$.

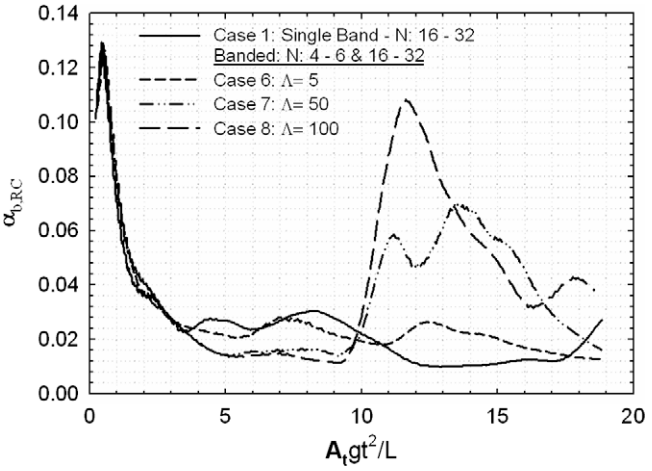

Fig. 12. Evolution of growth rate parameter for bubbles for case 1 (single band, N: 16–32) and cases 6–8 (double band, N: 4–6 and 16–32 with $A = 5$, 50 and 100, respectively).

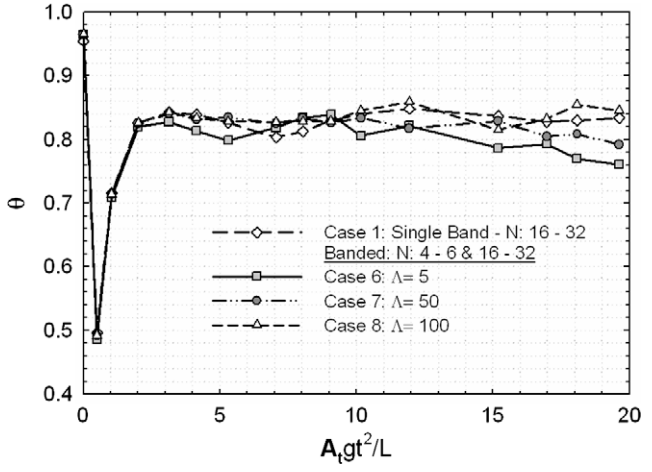

Fig. 13. Evolution of molecular mix parameter for case 1 (single band, N: 16–32) and cases 6–8 (double band, N: 4–6 and 16–32 with $A = 5$, 50 and 100, respectively).

Acknowledgements

A.B. thank the Supercomputing facility at Missouri S&T (NIC Cluster) for permitting use of their computing resources. M.J.A. acknowledges the support of the Los Alamos National Laboratory through the LDRD-DR office and project 20090058.

References

[1] Lord Rayleigh, Investigation of the equilibrium of an incompressible heavy fluid of variable density, Proc. Lond. Math. Soc. 14 (1884) 170–177.
[2] G.I. Taylor, The instability of liquid surfaces when accelerated in a direction perpendicular to their planes I, Proc. R. Soc. Lond. A 201 (1950) 192–196.
[3] M.J. Andrews, D.B. Spalding, A simple experiment to investigate two-dimensional mixing by Rayleigh–Taylor instability, Phys. Fluids A2 (1990) 922–927.
[4] C. Wunsch, R. Ferrari, Vertical mixing energy and the general circulation of oceans, Annu. Rev. Fluid Mech. 36 (2004) 281–314.
[5] J.F. Adkins, K. McIntyre, D.P. Schrag, The salinity temperature and δ^{18} O of the glacial deep ocean, Science 298 (2002) 1769–1773.
[6] D. Veynante, L. Vervisch, Turbulent combustion modeling, Prog. Energy Combustion Sci. 28 (2002) 193–266.
[7] D. Veynante, A. Trouvé, K.N.C. Bray, T. Mantel, Gradient counter-gradient scalar transport in turbulent premixed flames, J. Fluid Mech. 332 (1997) 263–293.
[8] R.E. Britter, S.R. Hanna, Flow and dispersion in urban areas, Annu. Rev. Fluid Mech. 35 (2003) 469–496.
[9] J.D. Lindl, Inertial Confinement Fusion: The Quest for Ignition and Energy Gain Using Indirect Drive, Springer, Berlin, 1998.
[10] S. Nakai, H. Takabe, Principles of inertial confinement fusion-physics of implosion and the concept of inertial fusion energy, Rep. Prog. Phys. 59 (1996) 1071–1131.
[11] S.F. Gull, The X-ray optical and radio properties of young supernova remnants, R. Astron. Soc. Mon. Not. 171 (1975) 263–278.
[12] S.A. Colgate, R.H. White, The hydrodynamic behavior of supernova explosions, Astrophys. J. 143 (1966) 626–681.
[13] S. Chandrasekhar, Hydrodynamic and Hydromagnetic Stability, second ed., Dover, New York, 1981.
[14] S.W. Haan, Onset of nonlinear saturation for Rayleigh–Taylor growth in the presence of a full spectrum of modes, Phys. Rev. A 39 (1989) 5812–5825.
[15] V.N. Gonchorov, Analytical model of nonlinear single-mode classical Rayleigh–Taylor instability at arbitrary Atwood numbers, Phys. Rev. Lett. (2002) 134502-1–134502-4.
[16] N.N. Anuchina, Y.A. Kucherenko, V.E. Neuvazhaev, V.N. Ogibina, L.I. Shibarshov, V.G. Yakovlev, Turbulent mixing at an accelerating interface between liquids of different densities, Izv Akad Nauk SSSR Mekh Zhidk Gaza 6 (1978) 157–160.
[17] D.L. Youngs, Numerical simulation of turbulent mixing by Rayleigh–Taylor instability, Physica D 12 (1984) 32–44.
[18] P. Ramaprabhu, M.J. Andrews, On the initialization of Rayleigh–Taylor simulations, Phys. Fluids 16 (2004) L59–L62.
[19] P. Ramaprabhu, G. Dimonte, M.J. Andrews, A numerical study on the influence of initial perturbations on the turbulent Rayleigh–Taylor instability, J. Fluid Mech. 436 (2005) 285–319.
[20] G. Dimonte, D.L. Youngs, A. Dimits, S. Weber, M. Marinak, S. Wunsch, C. Garasi, A. Robinson, M.J. Andrews, P. Ramaprabhu, A.C. Calder, B. Fryxell, J. Biello, L. Dursi, P. MacNeice, K. Olson, P. Ricker, R. Rosner, F. Timmes, H. Tufo, Y.N. Young, M. Zingale, A comparative study of the turbulent Rayleigh–Taylor (RT) instability using high-resolution 3D numerical simulations: the alpha-group collaboration, Phys. Fluids 16 (2004) 1668–1693.
[21] D.L. Youngs, Numerical simulation of Rayleigh–Taylor and Richtmeyer–Meshkov instabilities, Laser. Part. Beams 12 (1994) 725–750.
[22] W.H. Cabot, A.W. Cook, Reynolds number effects on Rayleigh–Taylor instability with possible implications for type-Ia supernovae, Nat. Phys. 2 (2006) 562–568.
[23] Y.N. Young, H. Tufo, A. Dubey, R. Rosner, On the miscible Rayleigh–Taylor instability: two and three dimensions, J. Fluid Mech. 447 (2001) 377–408.
[24] J. Glimm, J.W. Grove, X.L. Li, W. Oh, D.H. Sharp, A critical analysis of Rayleigh–Taylor growth rates, J. Comput. Phys. 169 (2001) 652–677.
[25] A. Banerjee, W.N. Kraft, M.J. Andrews, Detailed measurements of a Rayleigh–Taylor mixing layer from small to intermediate Atwood Numbers, J. Fluid Mech., 2008.
[26] P. Ramaprabhu, M.J. Andrews, Experimental investigation of Rayleigh–Taylor mixing at small Atwood numbers, J. Fluid Mech. 502 (2004) 233–271.
[27] G. Dimonte, M. Schneider, Density ratio dependence of Rayleigh–Taylor mixing for sustained and impulsive acceleration histories, Phys. Fluids 12 (2000) 304–321.
[28] M.J. Andrews, Accurate computation of convective transport in transient two-phase flow, Int. J. Numer. Method. Fluids 21 (1995) 205–222.
[29] M.J. Andrews, Turbulent Mixing by Rayleigh–Taylor Instability, Ph.D. Thesis, Imperial College of Science and Technology, London, 1986.
[30] S.V. Patankar, Numer. Heat Trans. Fluid Flow, second ed., Hemisphere, 1980.
[31] B. Van Leer, Towards the ultimate conservative difference scheme IV. A new approach to numerical convection, J. Comput. Phys. 23 (1977) 276–299.

[32] A.C. Robinson, J.W. Swegle, Acceleration instability in elastic–plastic solids II. Analytical techniques, J. Appl. Phys. 66 (1989) 2859–2872.
[33] J.W. Miles, J.K. Dienes, Taylor instability in a viscous fluid, Phys. Fluids 9 (1966) 2518–2519.
[34] J.R. Ristorcelli, T.T. Clark, Rayleigh–Taylor turbulence: self-similar analysis and direct numerical simulations, J. Fluid Mech. 507 (2004) 213–253.
[35] D.H. Sharp, An overview of Rayleigh–Taylor instability, Physica D 12 (1984) 3–10.
[36] A.W. Cook, P. Dimotakis, Transition stages of Rayleigh–Taylor instability between miscible fluids, J. Fluid Mech. 443 (2001) 69–99.
[37] K. Read, Experimental investigation of turbulent mixing by Rayleigh–Taylor Instability, Physica D 12 (1984) 45–58.
[38] P.V. Danckwerts, The definition and measurement of some characteristics of mixtures, Appl. Sci. Res. 3 (1952) 279–296.
[39] P.N. Wilson, M.J. Andrews, Spectral measurements of Rayleigh–Taylor mixing at low-Atwood number, Phys. Fluids A 14 (3) (2002) 938–945.
[40] D.L. Youngs, Application of MILES to Rayleigh–Taylor and Richtmyer–Meshkov mixing, 16th AIAA Computational Fluid Dynamics Conference, 2003, Paper No. AIAA 2003–4102.